



HAL
open science

On spreading modes and magma supply at slow and ultraslow mid-ocean ridges

Mathilde Cannat, Daniel Sauter, Luc L Lavier, Manon Bickert, Ekeabino Momoh, Sylvie Leroy

► To cite this version:

Mathilde Cannat, Daniel Sauter, Luc L Lavier, Manon Bickert, Ekeabino Momoh, et al.. On spreading modes and magma supply at slow and ultraslow mid-ocean ridges. *Earth and Planetary Science Letters*, 2019, 519, pp.223-233. 10.1016/j.epsl.2019.05.012 . hal-02325314

HAL Id: hal-02325314

<https://hal.science/hal-02325314>

Submitted on 25 Nov 2020

HAL is a multi-disciplinary open access archive for the deposit and dissemination of scientific research documents, whether they are published or not. The documents may come from teaching and research institutions in France or abroad, or from public or private research centers.

L'archive ouverte pluridisciplinaire **HAL**, est destinée au dépôt et à la diffusion de documents scientifiques de niveau recherche, publiés ou non, émanant des établissements d'enseignement et de recherche français ou étrangers, des laboratoires publics ou privés.

1 ON SPREADING MODES AND MAGMA SUPPLY AT SLOW AND ULTRASLOW MID-OCEAN RIDGES

2
3 Mathilde Cannat¹, Daniel Sauter², Luc Lavier³, Manon Bickert¹, Ekéabino Momoh¹⁻⁴, Sylvie Leroy⁴

4 ¹ Marine Geosciences, Institut de Physique du Globe de Paris, UMR 7154 - CNRS, Université de Paris

5 ² Institut de Physique du Globe de Strasbourg, UMR 7516 - CNRS, Université de Strasbourg.

6 ³ Department of Geological Sciences, Institute for Geophysics, Jackson School of Geosciences, The
7 University of Texas at Austin

8 ⁴ Institut des Sciences de la Terre de Paris, UMR 7193 - CNRS, Sorbonne Université

9
10 **ABSTRACT**

11 The ultraslow eastern Southwest Indian Ridge (SWIR) offers an opportunity to study the effect of
12 magma supply on an ultraslow mid-ocean ridge starting from quasi-melt-free detachment-dominated
13 spreading, and transitioning to volcanic spreading as one nears prominent axial volcanos. Detachments
14 in the quasi-melt-free mode extend along-axis 60 to 95 km and have a lifetime of 0.6 to 1.5 myrs. They
15 cut into their predecessor's footwall with an opposite polarity, causing part of the footwall lithosphere
16 to experience further deformation, hydrothermal alteration, sparse magmatism and possibly thermal
17 rejuvenation, in a hanging wall position. The accretion of the oceanic lithosphere in this context
18 therefore occurs in two distinct stages over the lifetime of two successive detachment faults. We
19 examine the transition from this nearly amagmatic detachment-dominated mode to the more
20 common volcanic mode of spreading, showing that it occurs along-axis over distances ≤ 30 km. It
21 involves a significant thinning of the axial lithosphere and a gradual decrease of the amount of tectonic
22 displacement on faults, as the magmatic contribution to the divergence of the two plates increases.
23 We develop a conceptual model of this transition, in which magma plays a double role: it fills the space
24 between the diverging plates, thus reducing the need for displacement along faults, and it modifies
25 the thermal state and the rheology of the plate boundary, affecting its thickness and its tectonic
26 response to plate divergence. Based on a comparison of the ultraslow eastern SWIR, with the faster
27 spreading Mid-Atlantic Ridge, we show that the activation of the volcanic, or of the detachment-
28 dominated modes of spreading is connected with the volume of magma supplied per increment of
29 plate separation, over a range of axial lithosphere thickness, and therefore over a range of the M ratio
30 defined by (Buck et al., 2005) as the relative contribution of magma and faults to plate divergence (M
31 is smaller, for a given volume of melt per increment of plate separation, if the plate is thicker). We
32 therefore propose that M does not fully explain the variability in faulting styles observed at slow and

33 ultraslow ridges and propose that rheological changes induced by magma (melt itself is weak,
34 hydrothermally altered gabbro-peridotite mixtures are weak, and melt heat sustains more vigorous
35 hydrothermal circulation) also play a key role, resulting in contrasted potentials for strain localization,
36 footwall flexure on faults and the development of detachment faults.

37

38 **Keywords:** slow and ultraslow mid-ocean ridges, divergent plate boundaries, detachment faults, melt
39 supply, axial lithosphere, tectonic and magmatic seafloor spreading processes

40

41 INTRODUCTION

42 While all mid-ocean ridges are active volcanic chains, slow (<4 cm/yr) and ultraslow (<2 cm/yr)
43 spreading ridges are also rift zones, where normal faults accommodate part of the plate divergence,
44 interacting with magmatism to shape the newly formed oceanic lithosphere. These ridges are
45 segmented, and significant along-axis variations in melt supply accompany this segmentation, with
46 segment ends receiving less magma than the segments centers (Lin et al., 1990). At segment ends, and
47 in whole segments of melt-poor slow and ultraslow ridge regions, large offset normal faults, also called
48 detachment faults, accommodate a large part of the plate divergence (Cann et al., 1997; Cannat et al.,
49 2006; Escartín et al., 2008; Sauter et al., 2013). These detachments bring mantle-derived rocks up
50 through the axial lithosphere, and the resulting seafloor therefore has an ultramafic, non-magmatic
51 component (Cannat, 1993). By contrast, the centers of most slow and ultraslow spreading ridge
52 segments undergo plate divergence through a combination of magma injection and several moderate
53 offset normal faults distributed in the axial domain, and the seafloor exposes volcanic rocks (Smith and
54 Cann, 1999). In the detachment-dominated mode of spreading, specific hydrothermal reactions,
55 associated with the alteration of mantle peridotites, are favored, and feed original microbial
56 communities (Früh-Green et al., 2004). Modes of spreading at slow and ultraslow spreading ridges
57 therefore have a large impact not only on the composition of the oceanic lithosphere, but also on
58 chemical exchanges between the solid Earth and the Ocean, and on the diversity of seafloor biology.

59 Many questions remain about oceanic accretion in the detachment-dominated mode. What controls
60 the geometry and lifetime of detachments, and how do they root into the mantle? How do
61 hydrothermal and magmatic processes operate in this mode and what are their time and space
62 relations to detachment faulting? What is the architecture of the lithosphere that is accreted in the
63 hanging wall plate? Although it is often assumed to be better constrained, there is also a lot we do not
64 yet know about the volcanic spreading mode at slow and ultraslow ridges. While crustal architecture
65 in this mode is commonly proposed to be similar to the layered magmatic crust formed at fast ridges,

66 there is as yet limited direct evidence in support of this hypothesis, and at least one indication that it
67 might not be the case: while volcanic slow spreading ridge regions have a substantial magma supply,
68 they also have a much thicker (up to 7 km-thick at the Mid-Atlantic Ridge; Wolfe et al., 1995)
69 seismogenic lithosphere, compared with the shallow depth to the axial melt lens of faster ridges
70 (Detrick et al., 1987). Finally, while magma supply is identified as a main control on which of the two
71 spreading modes is activated at slow and ultraslow spreading ridges, and although this control has
72 been tested in numerical models (Buck et al., 2005; Olive et al., 2010; Püthe and Gerya, 2014; Tian and
73 Choi, 2017; Tucholke et al., 2008), there is no clear understanding as yet on how it operates in situ: by
74 what melt supply-related mechanism(s) does a slow spreading ridge switch from the volcanic to the
75 detachment-dominated mode of spreading?

76 We address several of these questions based on geological, geophysical and petrological data acquired
77 over the course of several cruises in the eastern region of the Southwest Indian Ridge (SWIR; spreading
78 rate of 14 mm/yr; Cannat et al., 2006), east of the Melville Fracture Zone. This 660 km-long ridge region
79 is a low magma supply end-member of the global mid-ocean ridge system (Cannat et al., 2008). It is
80 characterized by a pronounced focusing of the available melt to axial volcanos, separated by corridors
81 of nearly-amagmatic detachment-dominated spreading where the seafloor exposes almost only
82 ultramafic rocks (Cannat et al., 2006; Sauter et al., 2013). Volcanic areas show numerous and mostly
83 spreading-perpendicular scarps and hummocky volcanic ridges, and correspond to more negative
84 gravity anomalies, consistent with seismic crustal thicknesses up to 8 km (Minshull et al., 2006). Nearly
85 amagmatic spreading corridors have, by contrast, a smooth topography, more positive gravity
86 anomalies (Cannat et al., 2006), and a 2 to 5 km-thick seismic crustal layer that is interpreted as made
87 primarily of serpentinized and fractured mantle-derived rocks (Momoh et al., 2017). These rocks are
88 proposed to have been exhumed by successive axial detachment faults, each cutting into the footwall
89 of the previous fault, with an opposite polarity (Sauter et al., 2013). The eastern SWIR therefore offers
90 opportunities to study the links between magma supply and seafloor spreading modes starting from a
91 quasi melt-free regime, and transitioning to volcanic spreading as one nears the axial volcanos.

92 The formation of many distal continental divergent margins also involves tectonic extension with only
93 incipient magmatism (eg Peron-Pinvidic et al., 2013). Specifically, seismic reflectors imaged in the
94 Ocean Continent Transition (OCT) of the Iberian and Australian margins may also have formed by
95 detachment faults that alternated polarity (Gillard et al., 2015; Reston and McDermott, 2011).
96 Divergence rates and melt supply during the OCT phase, and during the following onset of indisputable
97 seafloor spreading at these margins, are not strongly constrained. Our results and hypothesis on the
98 nearly amagmatic seafloor spreading mode, and on its transition to volcanic seafloor spreading at an

99 ultraslow ridge, may nonetheless inform studies of detachment-dominated divergence and mantle
100 exhumation at the OCT phase, and of the transition from OCT to true seafloor spreading.

101

102 **RESULTS**

103 **Along-axis extension, and estimated lifetime of successive axial detachments in a nearly amagmatic** 104 **eastern SWIR spreading corridor**

105 We focus on the nearly amagmatic corridor between the 64°E and 65.6°E axial volcanos (Figure 1). The
106 smooth seafloor there forms 500 to 1000 m-high broad ridges, parallel to the ridge axis, which is nearly
107 orthogonal to the north-south trending direction of plate divergence to the west of 65°E, and up to
108 25° oblique to the east (Figure 1). Following (Sauter et al., 2013), we interpret these broad ridges
109 (numbered from 1 to 8 going back in time; Figure 1) as formed by successive axial detachments
110 between about 11 myrs-ago (#8) and the present (#1). The along flowline profile in Figure 2
111 summarizes this tectonic interpretation. Axial detachments #6 (which we propose was initiated about
112 5.6 myrs ago) to #1 (presently active) each cut into the footwall of the previous detachment, with an
113 opposite polarity (Sauter et al., 2013). Proposed breakaways B7 and B8 are both located in the
114 northern, African plate (Figures 1 and 2) and the corresponding exhumed fault surfaces locally bear
115 spreading-parallel corrugations (Cannat et al., 2009). These two south-facing detachments face
116 volcanic conjugate seafloor in the Australian plate and therefore formed under more magmatically
117 active axial conditions than detachments #6 to #1 (Cannat et al., 2009).

118 We pick the top of the inward-facing (toward the axis) slope of each ridge as the best approximation
119 (see Appendix Figure A1) for the location of the breakaway of the corresponding detachment fault,
120 and the base of the outward-facing slope of the corresponding broad ridge as the best approximation
121 for the location of the emergence of each fault at the seafloor. The along-axis extension of the eight
122 identified detachments, based on the length of their breakaway (Figure 1 and Table 1), ranges between
123 25 km (B7) and 95 km (B4). While these breakaways are mostly straight, the inferred emergence traces
124 show convex-outward undulations, with a typical wavelength of 15-20 km (Figure 1). These likely
125 reflect along-axis changes in the rheology of the detachment footwall, impacting the fault's emergence
126 angle. Most detachment-controlled ridges extend up to, and in the case of B5 (to the west) and B8 (to
127 the west and east), into, adjacent volcanic areas (Figure 1). Breakaway ridges B4, and to a lesser extend
128 B2, in the Antarctic plate, are long and follow the overall trend of the ridge axis, curving from E-W in
129 the west, to ENE-WSW in the east (Figure 1). Breakaway ridges B5 and B7, in the African plate, are
130 shorter and relayed to the east by broad ridges that trend NE-SW, oblique to the N-S spreading
131 direction but parallel to the local trend of the ridge axis. A shorter ENE-WSW ridge, also interpreted as

132 a detachment fault block, is found in an intermediate position to the east of B3 and B5 (Figure 1). These
133 local complexities are interpreted as due to faulting modes specific to oblique nearly amagmatic
134 spreading (Sauter et al., 2013) and are beyond the scope of this paper. We thus focus the following
135 analysis and discussions on the orthogonal-spreading part of the smooth seafloor corridor, to the west
136 of 65°E (Figure 1).

137 The horizontal offset estimated for past detachments is the along-flowline distance between
138 breakaway and emergence (reconstructed at the time of initiation of the next detachment). For
139 detachment #1, which is still active and at an early stage, the proposed estimate takes mass-wasting
140 into account and is explained in Appendix Figure A1. Estimated horizontal offsets for detachments
141 along the 64.6°E flowline (Figure 2) range between 4 km (active detachment #1; Table 1), and ~21 km
142 (detachments #2 and #8). At a spreading rate of 14 mm/yr (Patriat and Segoufin, 1988), these
143 estimated horizontal offsets correspond to faulting durations (Table 1) between 300 kyrs (detachment
144 #1, still active) and 1.5 myrs (detachment #2) for nearly amagmatic detachments 1 to 6, and of about
145 2.8 myrs, for corrugated detachments 7 and 8. For nearly amagmatic, flipping polarity detachments #
146 1 to 6, the horizontal distance between the emergence of a detachment and the location of the next
147 breakaway is 2.8 to 5.6 km (Table 1), indicating that new detachments typically cut into footwall rocks
148 that had been exhumed 200 to 400 kyrs previously.

149

150 **Footwall to hanging wall: two stages in the generation of melt-starved oceanic lithosphere**

151 A consequence of having successive detachments of opposite polarity that cut into their predecessor's
152 footwall is that the inward-facing slopes of smooth seafloor breakaway ridges are made of material
153 that was initially accreted and transported off-axis as part of the footwall of a detachment fault (Stage
154 1), then became part of the hanging wall of the next detachment fault (Stage 2). The oceanic
155 lithosphere forming these inward-facing slopes is therefore predicted to have been generated in two
156 stages and over the lifetime of two successive detachment faults.

157 Stage 2 involves the residence of previously accreted ultramafic seafloor, in the axial valley region as
158 part of the hanging wall of the next axial detachment (Figure 3). Geological observations made in the
159 present-day axial valley near 64.6°E indicate that Stage 2 results in the formation of small offset normal
160 faults and of isolated volcanic patches and ridges, that are distributed in a > 10 km-wide axial valley
161 (Sauter et al., 2013 and Figure 4). Seismic refraction and reflection results obtained in the same area
162 (Momoh et al., 2017) show lower seismic velocities and several sub-horizontal and north-dipping
163 reflectors in the basement of this near-axis domain, consistent with distributed faulting, hydrothermal
164 alteration and magmatic intrusions in the hanging wall of active detachment #1.

165 The outward-facing slopes of smooth seafloor breakaway ridges record only Stage 1: they form in the
166 footwall of a detachment, and are then captured, and moved off-axis into the footwall of the next
167 (antithetic) detachment. Seafloor ages in the outward-facing slopes of detachment ridges therefore
168 probably increase toward the axis (Figure 3). By contrast, most of the seafloor forming the inward-
169 facing slopes of these ridges has probably been modified by Stage 2 axial valley tectonics,
170 hydrothermal alteration and sparse volcanism, over the lifetime of the next, antithetic detachment.
171 Seafloor spreading in the near absence of melt is therefore predicted to result in complex seafloor age
172 patterns at scales of a few tens of kilometers or less (Figure 3). At larger scales, seafloor ages do
173 nonetheless increase off-axis: pickings for the two best expressed magnetic anomalies in the area (3A
174 and 5; Figure 1) are accordingly consistent with the ages predicted in Table 1 for breakaways B6 and
175 B8.

176 This two-stage evolution has two predictable consequences, in addition to the generation of a complex
177 lithosphere geology. One is the potential for thermal rejuvenation of the deep lithosphere during Stage
178 2, as older portions of the footwall of the first detachment find themselves on-axis again in the hanging
179 wall of the next detachment. The other concerns the potential for nearly amagmatic oceanic
180 lithosphere to bear magnetic anomalies. Ultramafic rocks that may have acquired a remanent
181 magnetization upon serpentinization (eg Oufi et al., 2002) in the footwall of the first detachment,
182 would then be subjected to Stage 2 diking and volcanic eruptions in the hanging wall of the next
183 detachment. For example, this could lead to the overprinting of a serpentinization-related magnetic
184 signature recorded up to 2.9 myrs ago at depth in the footwall of detachment #3, by the magnetic
185 signature recorded in volcanic rocks erupted up to 300 kyrs-ago in the hanging wall of detachment #2
186 (Figure 3). This, in addition to the overall low magnetization of serpentinized peridotites (refs), helps
187 explain why the magnetic anomaly record is poor and ambiguous over the ultramafic seafloor of the
188 study area (Bronner et al., 2014).

189

190 **Along-axis transition from detachment-dominated to volcanic spreading**

191 Figure 5 shows the transition, in the near-axis region, between nearly amagmatic detachment-
192 dominated spreading (along-flowline profile 1), and more magmatic spreading near the 64°E axial
193 volcano (profiles 3 and 4). Profile 1 has an asymmetrical topography, and the seafloor there exposes
194 almost only serpentinized peridotite (Sauter et al., 2013). Faults in the axial valley floor have vertical
195 offsets <200m; volcanism is sparse, forming isolated ridges and patches, and both rock sampling
196 (Paquet et al., 2016; Sauter et al., 2013) and seismic imaging (Momoh et al., 2017) indicate that
197 magmatic rocks form a volumetrically minor part of the basement. Nearly all the plate divergence is

198 therefore currently accommodated by axial detachment #1. By contrast, profiles 3 and 4, less than 30
199 km to the west, are located fully within volcanic seafloor, with several volcanic ridges, and fault scarps
200 that have a maximum vertical throw of 1000 m (Figure 5c). The gravity anomalies are in the negative
201 range (Figure 5b), consistent with a thicker crust (Cannat et al., 2006), and we see no evidence in these
202 profiles that detachment #1 is continuing at depths beneath rafted blocks of volcanic seafloor (Reston,
203 2018; Reston and Ranero, 2012). The axial topography is symmetrical, and seafloor ages from magnetic
204 anomalies (Cannat et al., 2006) increase monotonically with distance to the axis (Figure 5c). These
205 characteristics are consistent with in situ eruption of the volcanics and are typical of seafloor spreading
206 at moderate melt supply, with plate divergence being partitioned into magma emplacement and fault
207 displacement distributed in the axial domain (eg Buck et al., 2005).

208 Profile 2 is in an intermediate position and cuts the western end of detachment #1 (Figure 5a). The
209 seafloor along this profile shows volcanic morphologies, with spreading perpendicular ridges that are
210 clearly in-situ volcanic constructions (Figure 4 and Sauter et al., 2013), and fault scarps ≤ 200 m-high
211 (Figure 5b); yet the gravity anomalies are in the positive range (Figure 5b). These characteristics are
212 consistent with seafloor spreading at relatively low melt supply, with recent plate divergence being
213 accommodated for a part by detachment #1, and for another part by magma emplacement and smaller
214 offset normal faults distributed in the axial valley. The overall topography of the axial region along
215 profile 2 is distinctly asymmetrical across-axis and similar to that of profile 1. This asymmetric
216 topography is probably mostly due to the broad plate bending effect of the active detachment in the
217 nearly amagmatic eastern domain of profile 1. The axial domain between profiles 2 and 1 is
218 characterized by several volcanic ridges (Figure 4), that formed by local eruptions, on older volcanic
219 seafloor in the west, and directly over ultramafic seafloor to the east (Sauter et al., 2013).

220 Our near-axis observations therefore point to a gradual transition, over an along-axis distance of less
221 than 30 km, from the detachment-dominated, nearly amagmatic mode of spreading, to a melt-
222 emplacement dominated, symmetrical, mode of spreading. Such a gradual transition indicates that the
223 amount and the distribution of tectonic displacement (one axial detachment, and/or several
224 distributed smaller offset normal faults) at slow spreading ridges are tuned with the melt supply at
225 scales <10 km, so as to complement the melt emplacement contribution to the divergence of the two
226 plates (Figure 6).

227

228 **DISCUSSION**

229 **Full lithosphere sketches of an ultraslow and magma-poor ridge**

230 Figure 6 illustrates the concept of a gradual transition from the magmatically robust volcanic spreading
231 mode, to nearly amagmatic, detachment-dominated spreading, with tectonic displacement on faults
232 being tuned over the width of the axial domain, to complement melt emplacement so that the two
233 plates diverge at the spreading rate that is imposed by far-field plate tectonics forces. This is similar to
234 the interpretation proposed by (MacLeod et al., 2009) for the along-axis transition from detachment-
235 dominated spreading to more volcanic ridge domains at 13°N on the Mid-Atlantic Ridge (MAR); and an
236 alternative to the rafting detachment model developed by Reston and Ranero (2012) and by Reston
237 (2018), in which axial detachments are proposed to continue at depth beneath rafted blocks of volcanic
238 seafloor at slow and ultraslow ridges. We discard this alternative interpretation because of clear
239 geological evidence that volcanic rocks in the study area were erupted in situ (Figure 4 and recent
240 submersible observations; Cannat et al., AGU abstract 2017).

241 Figure 6 shows the upper 10 kilometers of the axial domain. Microearthquake depths reported by
242 Schlindwein and Schmid (2016), indicate that the seismogenic lithosphere thickens over an along-axis
243 distance of less than 50 km, from less than 10 km-thick beneath the 65.6°E axial volcano (Figure 1), to
244 about 25 km-thick at the eastern edge of the 64.6°E nearly amagmatic corridor. Assuming that a similar
245 thickening occurs with distance from the 64°E volcano (Figure 1), we infer that the volcanic seafloor at
246 the longitude of profiles 3 and 4, and the nearly amagmatic seafloor at the longitude of profile 1
247 probably have seismogenic lithosphere thicknesses of about 10-15 km, and 20-25 km, respectively.
248 Transitioning from the two spreading modes therefore also involves thinning the axial seismogenic
249 lithosphere by at least 10 km, over an along-axis distance of ~30 km. In the following paragraphs, we
250 discuss full-lithosphere conceptual sketches based on the present-day geology of the eastern SWIR
251 axis, for the nearly amagmatic and for the volcanic spreading modes.

252

253 *Nearly amagmatic, detachment-dominated spreading mode.* Detachment #1 (Figure 1) presently
254 accommodates nearly all the plate divergence. It cuts through the thick axial brittle lithosphere and
255 roots into ductile shear zones that are documented in dredged ultramafic samples (Bickert et al., in
256 prep.) at the base of the plate (Figure 7a). This detachment is at an early stage (~300 kyrs of activity
257 for a typical detachment lifetime of 1 to 1.5 myrs; Table 1) and has so far caused an estimated
258 maximum footwall flexure of 15° (Appendix Figure A1). This flexure could at least partially be
259 accommodated by reactivation of former detachment #2, accounting for the change of slope observed
260 across the proposed emergence of detachment #2 (E2; Figures 1 and 7a). Sub-horizontal and dipping
261 seismic reflectors documented in the axial valley basement are interpreted as minor conjugate faults
262 and magmatic intrusions in the hanging wall of detachment #1, some of which fed the sparse basalt
263 patches observed at the seafloor (Momoh et al., 2017). These basalts are compositionally distinct from

264 those erupted in the nearby volcanic seafloor domains and, based on their composition, it is unlikely
265 that they erupted from dikes propagating along-axis from these volcanic domains (Paquet et al., 2016).
266 Seafloor imagery (Sauter et al., 2013 and Figure 4) and submersible observations (Cannat et al., AGU
267 abstract, 2017) indicate that most basalt patches are spatially associated with faults that guide melts
268 in the upper levels of the lithosphere (Figure 7a). Melt infiltrations, and dikes intruded at greater
269 depths and presumably for the most part into the footwall plate (Figure 7a) are also documented in
270 peridotites samples from the smooth seafloor domains (Paquet et al., 2016).

271 Faults and the associated damage also probably channel hydrothermal fluids, so that serpentinization
272 would occur for a good part in and next to the main axial detachment (Andreani et al., 2007; Rouméjon
273 and Cannat, 2014). Sample studies indicate that serpentinization at slow ridges is a multiphase
274 reaction, occurring for the most part in the most kinetically favorable temperature range of 200-350°C,
275 with an initial stage of formation of the serpentine mesh texture at low fluid-rock ratios, followed by
276 several stages of veining and recrystallization of the initial serpentine at higher fluid-rock ratio
277 (Andreani et al., 2007; Früh-Green et al., 2004; Rouméjon et al., 2014). Based on hypocenter depth
278 distribution in melt-poor domains next to the 65.6°E axial volcano, Schindwein and Schmid (2016)
279 proposed that serpentinization there initiates at depths of ~15 km below seafloor (Figure 7a).
280 Temperatures in the 200-350° C range could, however, also be found at shallower, near seafloor
281 depths in the upflow zone of high temperature, black smoker-type, hydrothermal circulation cells.
282 Such high temperature hydrothermal upflows have not been discovered so far in the area, and given
283 that magmatic rocks are scarce, they should not represent the dominant hydrothermal regime. Yet
284 black smoker-type circulations may develop transiently to cool isolated melt intrusions and trigger
285 episodes of rapid serpentinization in the surrounding ultramafic rocks, both in the footwall and in the
286 hanging wall plates (Figure 7a). Slower, lower temperature serpentinization, as yet not documented
287 by sampling, may also occur in the tectonically damaged footwall and hangingwall domains.

288 At the current early stage of activity of detachment #1, the axial lithosphere, which we infer formed in
289 the footwall of detachment #2 (Figure 3), is 0.6 to 1.5 myrs-old and could thus be thicker than if
290 controlled solely by the active balance between present-day on-axis heat supply and heat loss. Heat in
291 this spreading mode would be supplied primarily by conduction, by tectonic advection of hot mantle,
292 and by serpentinization reactions. Although advected and latent heat from the sparse melt intrusions
293 could support active black smokers, this efficient mode of hydrothermal cooling would be highly
294 episodic and most hydrothermal circulations would occur at lower fluid-rock ratio in tectonically
295 damaged domains. The resulting axial temperature gradient should therefore be nearly conductive
296 (Figure 7c). Over time and as detachment #1 accommodates more displacement, greater footwall
297 flexure will occur, lowering the fault emergence angle and causing enhanced internal deformation and

298 serpentinization. Also, because of the near-zero melt input, the detachment system should migrate in
299 the direction of the hanging wall and away from the axial region of higher heat input and thinner
300 lithosphere, ultimately favoring the initiation of a new detachment (Buck et al., 2005).

301

302 *More magmatically robust volcanic spreading mode.* The gravity-derived crustal layer on-axis at the
303 longitude of profiles 3 and 4 is 6 to 7 km-thick (Cannat et al., 2006). Plate divergence there thus
304 concerns an axial lithosphere that is thinner than in the nearly amagmatic setting sketched in Figure
305 7a, but still thicker than the crust. Hence, even if magmatic dikes and gabbro bodies do accommodate
306 most plate divergence in the upper lithosphere, plate divergence acting on the deeper axial lithosphere
307 still requires tectonic uplift of mantle material from the asthenosphere, and through-going melts may
308 form mechanically weak intrusions in this axial lithospheric mantle (Cannat, 1993). Melts intruded
309 higher up, into the brittle lithosphere, will also constitute weak zones while they cool, crystallize, and
310 release the heat necessary to fuel vigorous black smoker-type hydrothermal circulation (eg Lowell et
311 al., 2013). The axial lithosphere in this volcanic setting (Figure 7b) should therefore not just be thinner
312 than in the nearly amagmatic detachment-dominated setting. It should also have a different type of
313 geotherm (Figure 7c), with an upper brittle part that is more efficiently cooled by hydrothermal
314 convection cells, and a lower part that is kept weak and thin by frequent melt injections. Temperatures
315 in the upper domain are expected to be variable in space and time (Figure 7c), depending on the
316 activation and geometry of black smoker circulations.

317 Whether magmatic intrusions that form in the lithospheric mantle are subsequently uplifted into the
318 crust, or remain at deep levels of the new plate as it is transported off-axis, should depend on the
319 distribution and offset of axial faults. In Figure 7b, we propose that several of the symmetrically-
320 distributed axial normal faults observed in profiles 3 and 4 (Figure 5) root into the melt-intruded axial
321 lithospheric mantle, and may thus lift some of its components into the crust. The axial domain of melt
322 emplacement may thus be thinned by faults to produce the off-axis crust. Therefore, although the melt
323 supply is probably such that the crustal layer off-axis is primarily magmatic, we predict that some of
324 these magmatic rocks have initially been intruded in the lithospheric mantle, then tectonically uplifted
325 into the crust by successive moderate offset normal faults, together with small volumes of their host
326 mantle rocks. Exhumed mantle-derived rocks have actually been dredged in the volcanic seafloor
327 domain a few km to the north west of profile 4 (Sauter et al., 2013).

328 This calls for a discussion of the applicability of the popular M ratio concept to this, and to other thick
329 lithosphere axial settings. The M ratio as defined by Buck et al. (2005) describes the fraction of the
330 total extension of the brittle lithosphere accommodated magmatically; (1-M) is accommodated by

331 faults. If melt emplacement accommodates plate divergence over the full thickness of the brittle plate,
332 as modelled for slow-spreading ridges by Buck et al. (2005) and Tucholke et al. (2008), M is a direct
333 function of the melt flux (m) per increment of plate separation (m can be expressed as the cumulated
334 thickness of melt provided per increment of spreading). On the other hand, the M ratio does not
335 directly reflect m if melts are either also emplaced below the plate on-axis (the common case at fast
336 and many slow ridges), or emplaced only over a portion of a thick axial brittle plate (probably the
337 common case at ultraslow mid-oceanic ridges). Instead, M then also depends on the thickness of the
338 brittle lithosphere on-axis (H_B), and on the thickness of the domain of axial melt emplacement (H_M).
339 Olive et al. (2010) addressed this for the $H_M > H_B$ case by defining a second ratio, M_D for the contribution
340 of melt emplaced in the ductile domain. In the $H_M < H_B$ case, M can be expressed as m/H_B . In the
341 volcanic seafloor configuration of Figure 7b, this formula yields a M value of ~ 0.6 , for $H_B = 12$ km and
342 assuming that the off-axis crustal thickness (~ 7 km) is a good approximation for m (ie that this off-
343 axis crust is mostly free of mantle-derived peridotites, and that there is very little gabbro trapped in
344 the off-axis mantle lithosphere).

345

346 *Transition between the detachment-dominated and volcanic modes of spreading.* Profile 2 (Figure 5)
347 corresponds to an along-axis transition between the detachment-dominated (to the east) and volcanic
348 (to the west) modes of spreading. Seafloor imagery and sampling (Sauter et al., 2013) suggest that
349 plate divergence at this longitude occurs by a combination of displacement along the westward
350 continuation of detachment #1, along smaller offset normal faults in the axial valley, and by in-situ
351 magmatic injections forming prominent spreading-perpendicular volcanic ridges (Figure 4). As a result,
352 the geophysically-defined crustal layer should be more geologically composite than in the nearly
353 amagmatic smooth seafloor configuration (Figure 7a), with proportions of serpentinized ultramafic
354 rocks and magmatic intrusions that would depend both of recent magmatic input, and of whether the
355 axial configuration in the recent past was more magmatic (in which case the crust offset by detachment
356 #1 would be mostly magmatic), less magmatic (in which case this crust would be mostly ultramafic) or
357 similarly magmatic.

358 In this intermediate spreading configuration, more melts would transit through and react with the
359 lower lithospheric axial mantle than in the nearly amagmatic configuration. These deep melts would
360 slowly release their intrinsic and latent heat into the surrounding mantle and would therefore keep
361 the lower axial lithosphere thinner and hotter than in Figure 7a. A further increase in the melt supply
362 would eventually allow for axial faults (and for the hydrothermal systems that develop in permeable
363 brittle rocks) to reach down to very near these melt-rich and hot regions, leading to vigorous
364 hydrothermal circulation. This configuration would ultimately resemble the more magmatically robust

365 volcanic mode of Figure 7b. This leads us to conclude that the effect of melts emplaced in thick
366 lithosphere, ultraslow spreading ridge settings goes beyond the mere mechanical accommodation of
367 plate divergence. Melts thin and weaken the lithosphere (thereby modifying the thickness and
368 strength of the rigid domain in which plate separation needs to be accommodated). Melts emplaced
369 in and near the brittle lithosphere also modify the axial thermal regime by fueling vigorous, if transient,
370 hydrothermal circulation, so that the upper and lower lithosphere are maintained at temperatures
371 respectively cooler and hotter than the conductive geotherm. We propose that these combined effects
372 (rheological and thermal) are key to understand how the two highly contrasted ridge settings proposed
373 in Figure 7 transition along-axis over distances <30 km.

374

375 **Spreading rate, melt supply, and the spreading mode at slow and ultraslow ridges**

376 Spreading rate has a large impact on the thermal regime of mid-ocean ridges (eg Chen and Morgan,
377 1990). With a spreading rate about half of that of the MAR, the SWIR is expected to have a thicker axial
378 lithosphere in places where the melt budget per unit of plate separation is the same, and a fortiori also
379 in places where this melt budget is less (the axial lithosphere should be even thicker due to a lesser
380 input of magmatic heat). In thick axial lithosphere settings, lithosphere thickness affects the (M) ratio
381 between the magmatic and tectonic contributions to plate separation and could therefore be expected
382 to be one of the main factors controlling the spreading mode (Buck et al., 2005). We now assess this
383 effect through a comparison of well-studied axial configurations at the MAR and SWIR.

384 The nearly amagmatic flip-flop detachment (after the terminology of Reston and McDermott, 2011)
385 mode documented at the ultraslow SWIR has not so far been identified at slow ridges, an absence that
386 probably results from more extreme degrees of along-axis melt focusing at ultraslow ridges, another
387 consequence of having a very thick axial lithosphere (Cannat et al., 2003; Standish et al., 2008). The
388 other two modes of slow spreading accretion (volcanic and corrugated detachment modes) are
389 common to both slow and ultraslow settings and therefore offer points of comparison. Microseismicity
390 results acquired at 13°N at the Mid-Atlantic Ridge, and in the 49°E region of the SWIR indicate
391 seismogenic lithosphere thicknesses of up to 15 km and 20 km respectively (Parnell-Turner et al., 2017;
392 Yu et al., 2018). Corrugated, dome-shaped, core-complexes that form in the Antarctic plate at 49°39'E
393 on the SWIR (Zhao et al., 2013), therefore result from detachments that cut through some 20 km of
394 brittle lithosphere, compared to up to 15 km for the 13°N MAR detachments (Figure 8). In the two
395 cases, domal exposed detachment surfaces face volcanic seafloor in the other plate (MacLeod et al.,
396 2009; Zhao et al., 2013), and seismic crustal thicknesses are similar (with a large 2-5 km range of
397 variation in the two settings). There is therefore no evidence for a significant contrast between the

398 two settings in terms of the volume of melt supplied per increment of plate separation. Along the same
399 line, the volcanic axial configuration in profiles 3 and 4 of Figure 4 resembles that observed at MAR
400 segment centers, with a symmetrical topography, distributed faults and a crustal thickness of 6-7 km,
401 yet it has an axial seismogenic plate thickness that is probably greater (10 to 15 km; Schlindwein and
402 Schmid, 2016) than documented for volcanic domains of the MAR (less than 8 km; Wolfe et al., 1995),
403 and more similar to that of corrugated detachment MAR domains (Figure 8).

404 These comparisons therefore suggest that the activation of the volcanic, or of the corrugated mode of
405 spreading at slow and ultraslow ridges is connected more to the volume of melt per increment of plate
406 separation, than to the thickness of the axial lithosphere. This is not fully consistent with the
407 hypothesis, proposed by (Buck et al., 2005), that spreading modes are determined by the relative
408 contribution of magma and faults to plate divergence, expressed as the M ratio. M is less, for a given
409 magmatic contribution m (the cumulated thickness of melt provided to the ridge per increment of
410 spreading), if the axial brittle plate is thicker. The volcanic and corrugated modes therefore both
411 appear to be activated at lower M at ultraslow than at slow ridges. The explanation we now explore is
412 that the impact of the axial lithosphere on spreading modes at slow and ultraslow ridges lies not just
413 in its actual thickness, but also in its strength, and that this strength is affected by melt supply.

414 Detachment-dominated modes, corrugated or not, develop for substantial lithosphere thicknesses
415 (Figure 8). MAR corrugated detachments are steep at depth (ca 70°; de Martin et al., 2007; Parnell-
416 Turner et al., 2017) but, when mature, emerge at very low angles (<15°; Smith et al., 2006), indicating
417 low effective footwall flexural rigidity. Smooth seafloor detachments in nearly amagmatic corridors of
418 the SWIR experience substantial, but probably not as large, footwall flexure (Momoh et al., in prep.).
419 Given that the axial lithosphere is not thin in either case, such large flexures call for mechanisms that
420 weaken the detachment footwall as faulting proceeds, forming weaker domains in an otherwise thick
421 mechanical lithosphere (Buck, 1988; Lavier et al., 1999). Most slow spreading ridge numerical models
422 to date have implemented this effect by making rock strength a function of strain (Lavier et al., 1999).
423 Geological ground truth comes from studies of samples from the exposed footwall of axial
424 detachments. These studies show that strain localization occurs primarily in assemblages of one or
425 several weak hydrous minerals (serpentine, chlorite, amphibole and talc; Boschi et al., 2006; Escartín
426 et al., 2003; Picazo et al., 2012; Schroeder and John, 2004) that form in the hydrothermally altered
427 brittle lithosphere, at greenschists facies temperatures (<500°C). Talc, specifically, is significantly
428 weaker than serpentine, and is not formed in substantial amounts from peridotites without the input
429 of additional silica, via metasomatic hydrothermal fluids that have altered magmatic rocks, or directly
430 from magmatic veins intruded in the peridotites (Boschi et al., 2006; Picazo et al., 2012). Talc is
431 uncommon in samples from the nearly amagmatic smooth seafloor (Rouméjon et al., 2014). It is by

432 contrast common in samples from corrugated seafloor. Large footwall flexure in the corrugated
433 detachment mode is therefore likely facilitated by talc forming from peridotite gabbro mixtures, while
434 nearly amagmatic detachments would operate with more rigid footwalls (Cannat et al., 2009). Higher
435 melt supply, leading to a transition from the corrugated detachment to the volcanic mode, would also
436 likely strengthen the brittle lithosphere (Cannat et al., 2009) because: 1- the proportion of mantle-
437 derived peridotites would become too small to form pervasive serpentine and or talc-bearing zones of
438 weakness; and 2- new magmatic intrusions, which initially form weak melt-mush and ductile gabbro,
439 turn, as they cool, into pristine and strong brittle magmatic rocks (Figure 8). More abundant melt, by
440 contrast, weakens the ductile axial lithosphere. The nearly amagmatic detachment mode is therefore
441 expected to be distinct from both the corrugated detachment, and the volcanic mode, in that it
442 operates with a significantly stronger lower axial lithosphere (Figure 8), which would oppose large
443 flexure and may therefore prevent the development of detachments (Lavie, 2002). Field evidence that
444 detachments exist in the SWIR nearly amagmatic spreading corridors indicates that additional strain
445 weakening mechanisms are activated. Microstructures in ductile and semi-brittle shear zones in
446 dredged ultramafic samples show that dynamic grain size reduction in the ductile mantle lithosphere
447 is a plausible candidate (Bickert et al., submitted).

448

449 **CONCLUSIONS**

450 We propose the following conclusions:

451 1- new oceanic lithosphere in the nearly amagmatic detachment-dominated mode is accreted over the
452 lifetime of two successive detachment faults (ie over 1.5 to 3 myrs) and is for the most part made of
453 material that experienced a two-stages tectonic, hydrothermal, and magmatic evolution: first in the
454 footwall of one detachment fault, then in the hanging wall of the next detachment fault.

455 2- individual active detachments extend over the whole along-axis width of nearly amagmatic seafloor
456 spreading corridors, up to 95 km in the case studied here. They accommodate up to 20 km of plate
457 divergence, and probably cut through a very thick axial lithosphere (≥ 25 km). Breakaways are straight,
458 cutting into ultramafic seafloor that was exhumed up to 400 kyrs previously in the former detachment
459 fault's footwall. The emergence of mature detachment faults shows 15-20 km-long undulations, which
460 we propose are due to along-axis changes in the rheology of the detachment footwall, impacting the
461 fault's emergence angle.

462 3- the along-axis transition from nearly amagmatic, detachment-dominated spreading, to more
463 magmatic spreading next to axial volcanic centers, occurs gradually over distances of < 30 km through
464 a fine tuning of tectonic displacement on faults to the local rates of melt emplacement, so as to

465 accommodate the plate divergence. We propose that this gradual transition involves two main
466 processes that are both related to the increase of melt supply: 1- more melt reduces the need for
467 displacement on faults as a mean to accommodate plate divergence; 2- more melt heats and weakens
468 the deep axial lithosphere, thus reducing the thickness of the rigid domain over which divergence
469 needs to be accommodated.

470 4- A comparison with the slow spreading MAR further suggests that the activation of the volcanic or
471 detachment-dominated modes of spreading at slow and ultraslow spreading ridges is primarily
472 controlled by the melt budget (the volume of melt supplied per unit of plate separation), over a range
473 of axial lithosphere thickness (the thickness of the plate over which divergence must be
474 accommodated, decreasing with spreading rate at a given melt budget). Spreading modes are
475 therefore not determined solely by the relative contribution of magma and faults to plate divergence
476 (the M ratio of Buck et al., 2005), since this relative contribution also depends on axial lithosphere
477 thickness . We propose that the rheology of the axial lithosphere is a key additional parameter, that
478 also depends on the melt supply. Melt and melt products modify the strength of the brittle lithosphere,
479 resulting in contrasted potential for strain localization and footwall flexure, the strongest configuration
480 being that of the most magmatically active (volcanic) mode, and the weakest and most favorable to
481 long-lasting detachments and large flexure, being that of the moderately magmatic (corrugated)
482 detachment mode. Melt heat can also sustain vigorous, black smoker type hydrothermal circulations
483 that impact the thermal state of the lithosphere and may favor enhanced hydrothermal alteration.
484 Finally, the presence of melt weakens the ductile mantle at the base of the brittle plate, so that the
485 nearly amagmatic detachment mode probably operates on axial domains that are characterized by a
486 strong ductile lithospheric mantle that is lacking in the more magmatically active corrugated
487 detachment and volcanic modes of spreading.

488

489 Acknowledgements:

490 We thank our two reviewers for their work and several helpful comments. We acknowledge partial
491 funding by CNRS-INSU post cruise research grants obtained in 2015 and 2017 and by ANR
492 project "Ridge-Factory-Slow". This is IGP paper #4025.

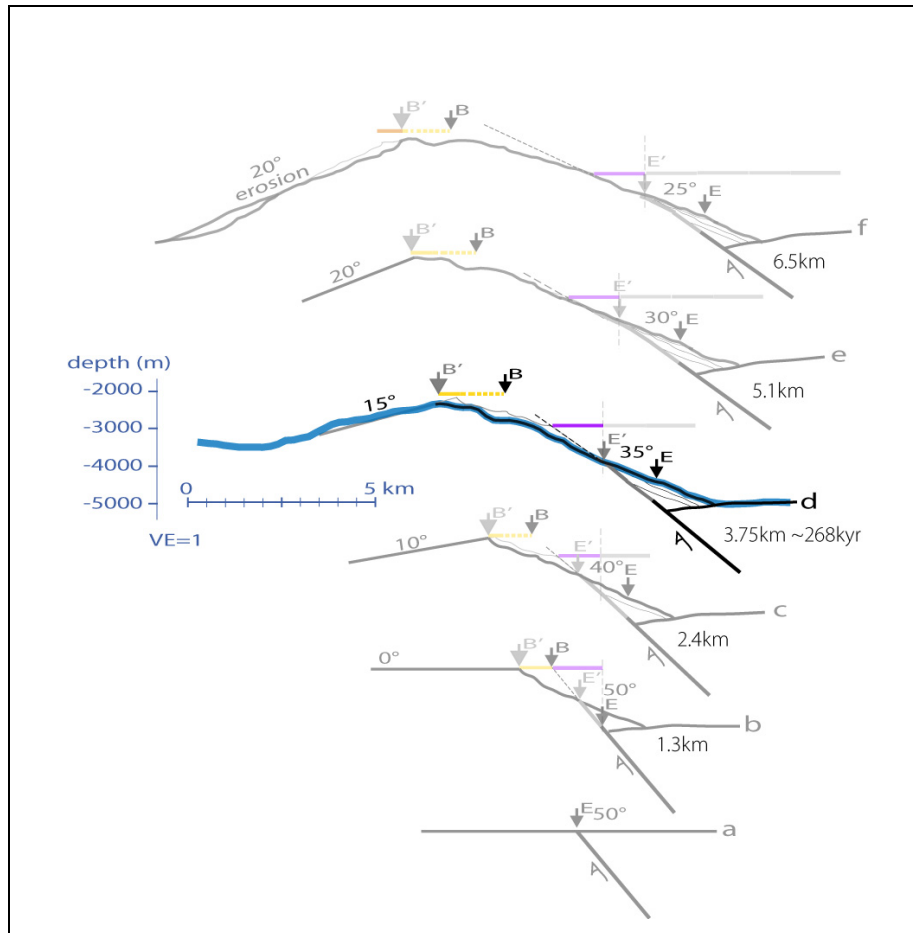
493

494 APPENDIX

495 **Mapping of axial detachment faults and estimating their age and lifetime in melt-poor oceanic**
496 **lithosphere**

497 In order to map past detachment faults in the nearly amagmatic spreading corridor of Figure 1, and to
498 estimate their age and lifetime (Table 1), we picked the top of the inward-facing (toward the axis) slope
499 of each detachment-controlled ridge as the best approximation for the breakaway, and the base of
500 their outward-facing slope as the best approximation for the emergence. This approach yields
501 uncertainties, primarily due to the effect of landslides, as illustrated in Figure A1 for presently active
502 detachment #1. For young detachments, the (eroded) breakaways (B in Figure A1) may be a few
503 hundred meters closer to the ridge axis than the top of the inward-facing slope of the detachment
504 ridge, but this discrepancy should diminish and eventually disappear as flexure proceeds so that the
505 outward facing slope of the detachment ridge steepens and also gets subjected to landslides (Figure
506 A1f). Similarly, the emergence of an active detachment may be several hundred meters closer to the
507 breakaway than the base of the detachment-controlled axial relief, which may correspond instead to
508 the front of landslide deposits (Figure A1d). For past detachments, however, this domain has been
509 captured into the footwall of a more recent detachment, probably causing flexure-related deformation
510 and further obscuring the relation between the base of the slope and the past location of the
511 emergence. We estimate that picking the emergence of past detachments at the base of the outward-
512 facing slopes is the most straightforward approach, although it may introduce errors of up to 2 km /
513 142 kyrs in the estimated displacement/duration of individual detachments. This is a large error on
514 individual detachments. However, because seafloor spreading in the study area has almost fully been
515 accommodated by detachment faulting from the initiation of detachment #6 (6.1 myrs ago; Table 1),
516 to the present, individual errors made with our method on each detachment must be compensated
517 on the others, within 2 km.

518



519 Figure A1. Conceptual sketches illustrating the evolution of presently active detachment #1. This
 520 detachment is at an early stage. Its proposed present-day configuration is shown in A1d, with the
 521 measured axial bathymetric profile in blue (no vertical exaggeration). The dip ($\sim 35^\circ$) and location of
 522 the emergence are based on recent submersible observations (Cannat et al., AGU abstract 2017).
 523 Panels A1c to A1a are back in time, and panels A1e to A1f into the near future, assuming a progressive
 524 footwall flexure, resulting in a decrease of the faults emergence angle from an initial 50° dip (although
 525 not shown, we assume that fault dips also increase with depth); and a 20° slope stability angle for
 526 serpentinites (Cannat et al., 2013), which is maintained at each step by landslides so that the eroded
 527 cross sectionnal area equals that of landslide deposits. B is the location of the actual breakaway, and
 528 B' is the location of the top of the ridge-ward slope at each step. The distance between B and B' results
 529 from mass-wasting and is expected to decrease with increasing offset and flexure along the
 530 detachment. E is the emergence of the fault with respect to the hanging wall plate, and E' is the
 531 emergence from the landslide package. Based on this sketch, our best estimate for the horizontal
 532 offset/duration of detachment #1 are about 4 km/300 kyrs (Table 1).

533

534

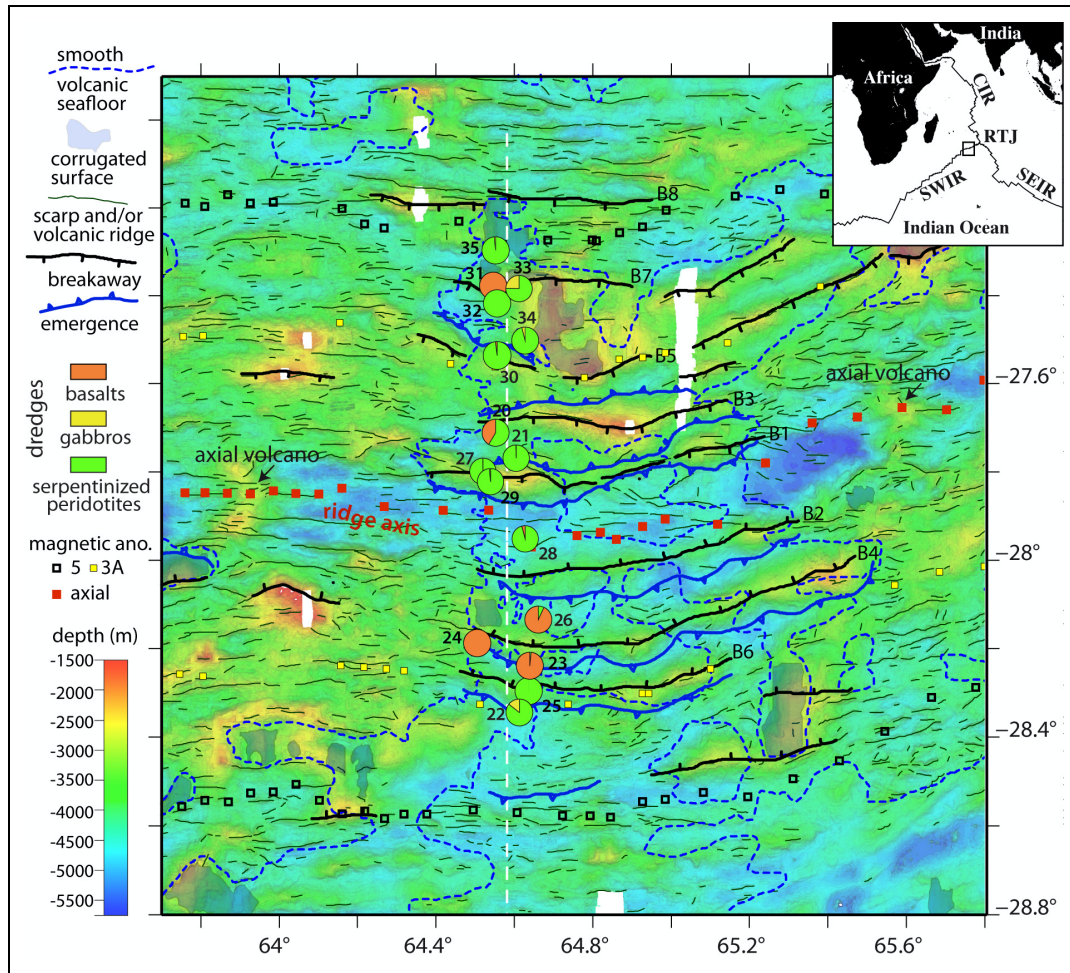
<u>detachment #</u>	<u>facing</u>	<u>along-axis extension at breakaway km</u>	<u>horizontal distance from emergence to breakaway km</u>	<u>horizontal distance from emergence to breakaway of next detachment km</u>	<u>Estimated total plate divergence km</u>	<u>estimated fault duration myr</u>	<u>age of breakaway myr</u>	<u>age of seafloor at breakaway myr</u>
1 (active)	south	85	(4)		(4)	(0.3)	(0.3)	(0.6)
2	north	75	21.0	4.2	21	1.5	1.8	2.2
3	south	60	16.2	5.6	16	1.1	2.9	3.1
4	north	95	14.0	2.8	14	1.0	3.9	4.3
5	south	60	15.1	4.7	15	1.1	5.0	5.2
6	north	60	9.3	3.2	9	0.6	5.6	6.1
7 (corrugated)	south	25	19.5	6.3	(39)	(2.8)	8.4	8.4
8 (corrugated)	south	45	20.6		(41)	(2.9)	(11.3)	(11.3)

536 TABLE 1. Characteristics of successive axial detachments as measured and estimated (see Appendix)
537 along the profile of Figure 2.

539

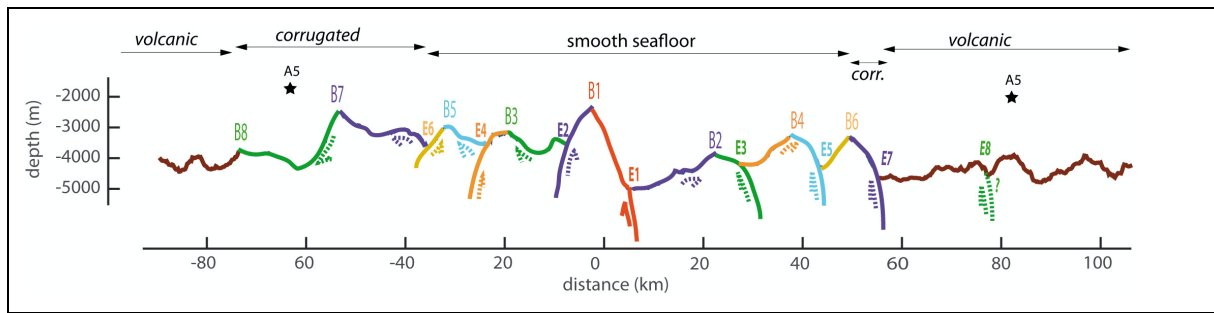
540 FIGURE CAPTIONS

541



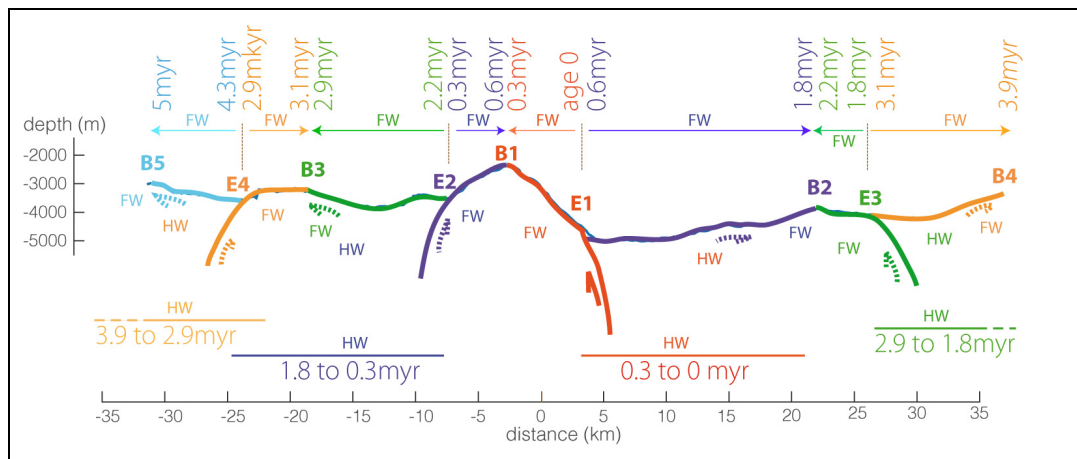
542 Figure 1. Tectonic sketch map showing the proposed breakaways and emergences of successive
543 detachments in the 64.6°E nearly amagmatic corridor; the volcanic scarps and ridges in the more
544 magmatically active volcanic domains to the east and west; the contours of these volcanic domains,
545 and of several corrugated detachment surfaces and pickings for magnetic anomalies 0, 3A and 5
546 (Cannat et al., 2006); the recovered lithologies in 16 dredges (Sauter et al., 2013); and the location of
547 the cross-section shown in Figure 2. Detachment faults breakaways (B) and emergences are numbered
548 from 1 (presently active) to 8 (initiated at the time of magnetic anomaly 5; ~11 Myrs ago).

549



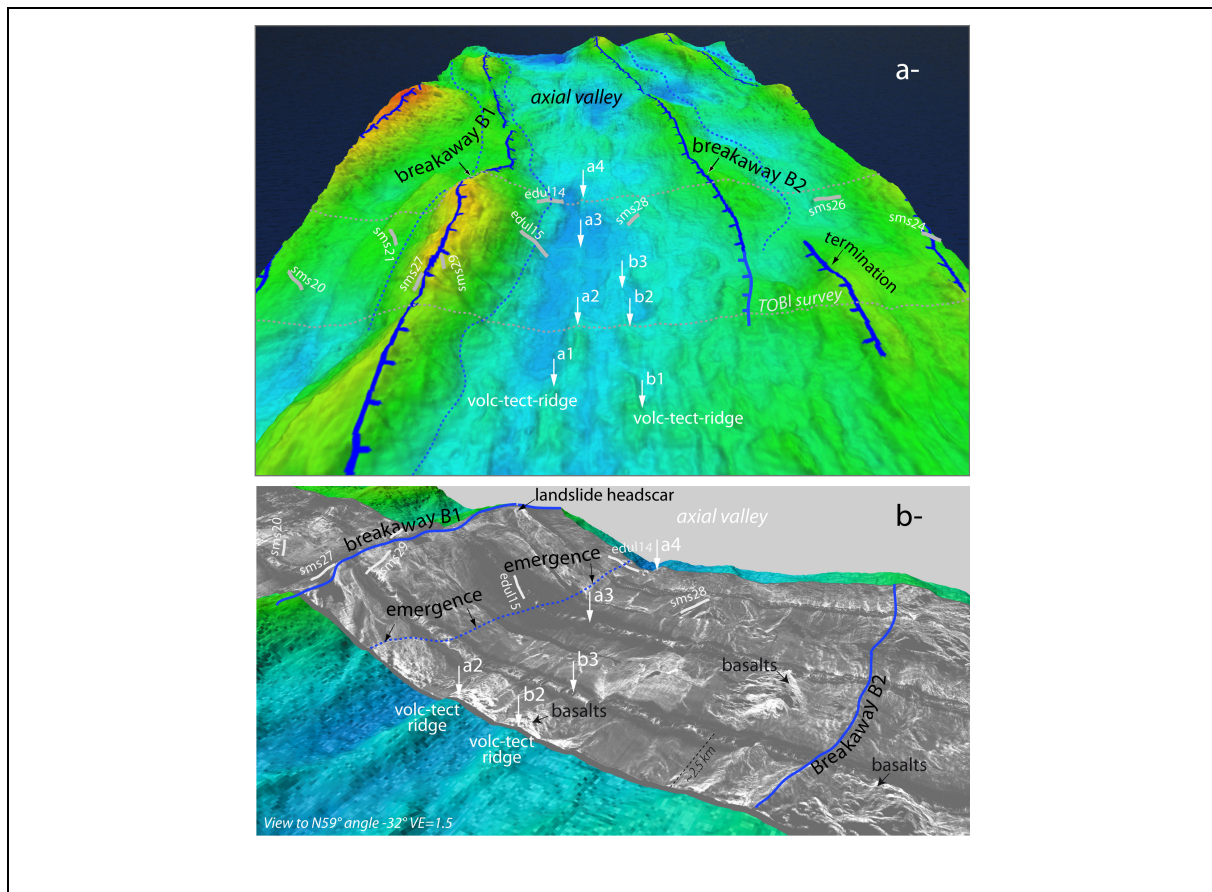
550 Figure 2. Tectonic interpretation of the along flowline cross-section located in Figure 1, modified after
 551 (Sauter et al., 2013), showing the proposed sequence of successive detachments leading to the
 552 continuous exposure of ultramafic rocks in the two diverging plates in smooth seafloor domain
 553 (detachments #6 to 1), or in the northern, African plate, facing volcanic seafloor in the Antarctic plate
 554 (corrugated-volcanic seafloor domains; detachments #8 and 7). Stars: pickings of anomaly A5 in
 555 nearest shipboard magnetic profile (Cannat et al., 2006).

556



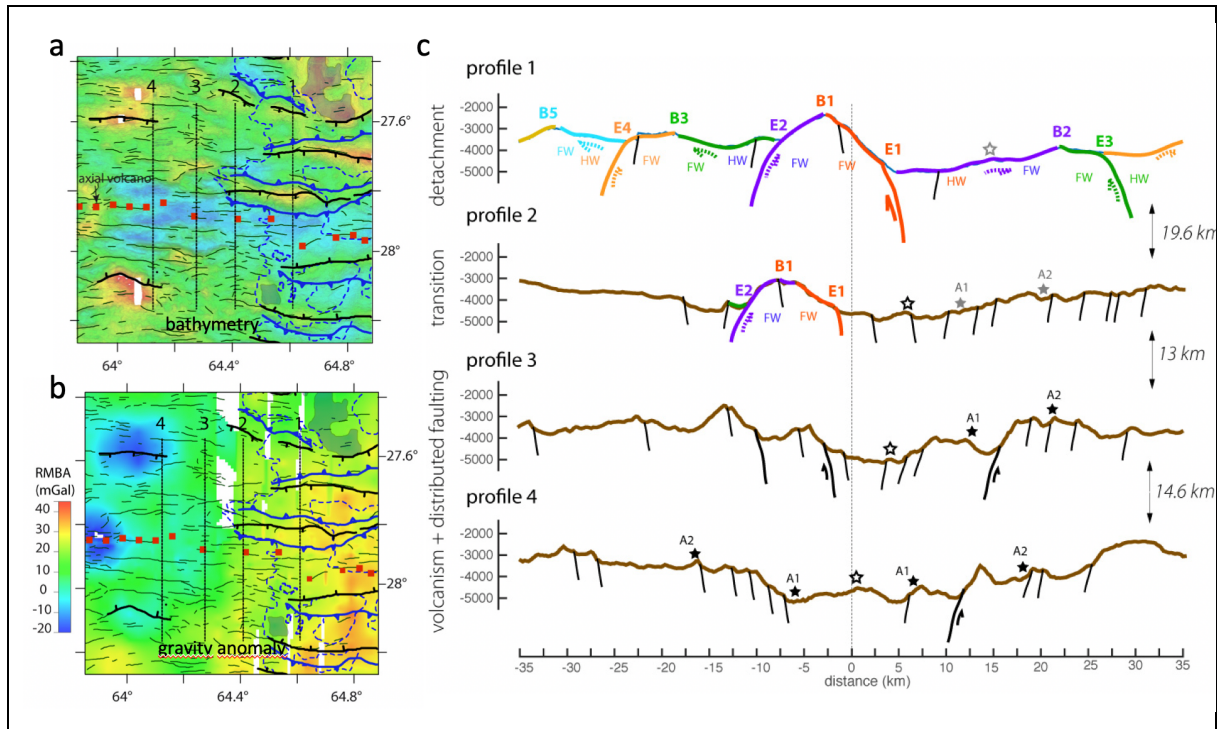
557 Figure 3. Tectonic interpretation of the along flowline cross-section located in Figure 1. Zoom to the
 558 near-ridge region, showing the ages estimated (text and Table 1) for the initial exposure of ultramafic
 559 rocks in the footwall (FW) of each detachment, and for subsequent tectonics, incipient volcanism, and
 560 hydrothermal alteration in the hanging wall (HW) of the next detachment.

561



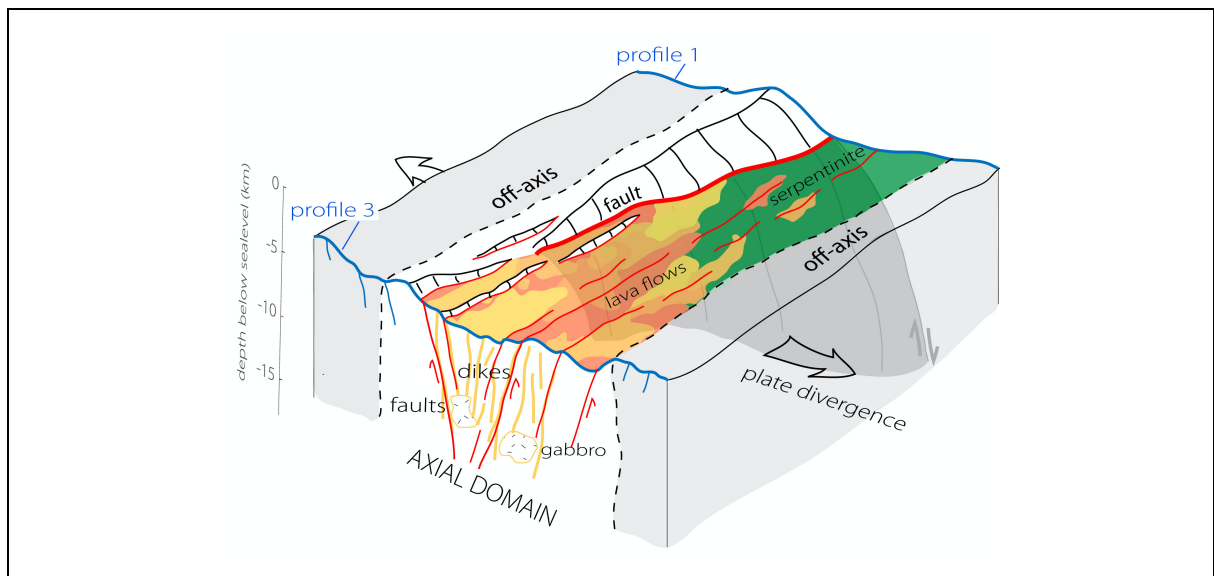
562 Figure 4. Perspective views of the near axis region in the 64.6°E nearly amagmatic corridor. a-
 563 bathymetry (depth scale as in Figure 1) with proposed detachment fault breakaways B1 and B2, dredge
 564 tracks (in grey, recovered rocks are > 90% ultramafic; (Sauter et al., 2013)), and outlines of the TOBI
 565 (Towed Ocean Bottom Instrument) survey (Sauter et al., 2013). b- TOBI reflectivity image drapped on
 566 bathymetry. Hummocky basaltic outcrops rest on less reflective ultramafic seafloor. They tend to form
 567 spreading-perpendicular ridges (a1-a2 and b1-b2), that align with small offset faults of the ultramafic
 568 basement (a2 to a4 and b2 to b3; these faults are more visible in the bathymetry of panel a). The
 569 location of the emergence of detachment #1 is based on recent submersible observations (Cannat et
 570 al., AGU abstract 2017).

571



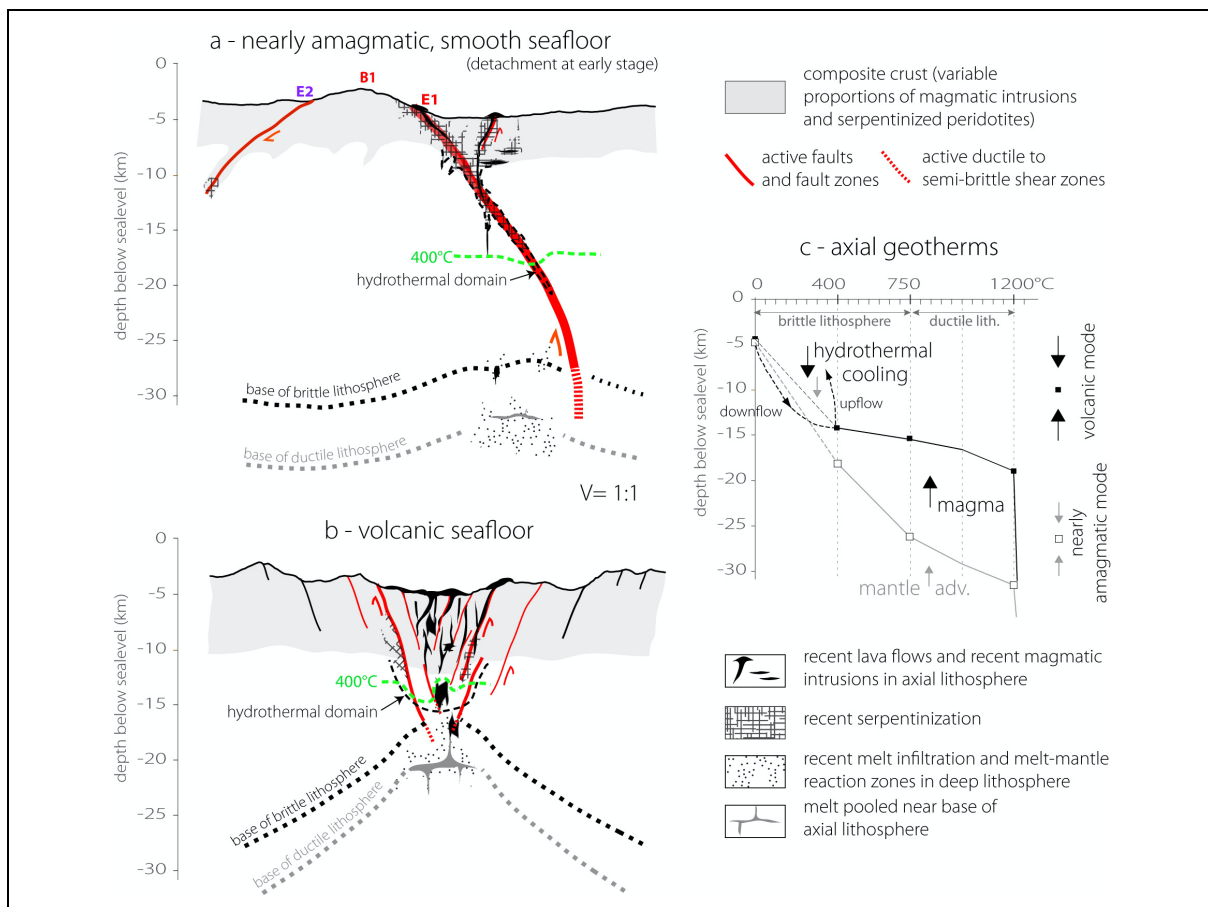
572 Figure 5. Tectonic interpretation of 4 along flowline cross-sections distributed over the transition from
 573 nearly amagmatic seafloor in the east (profile 1), to fully volcanic seafloor in the west (profiles 3 and
 574 4). Panels a and b show the location of these profiles on bathymetry (depth scale, tectonic features
 575 and axial magnetic anomaly pickings as in Figure 1) and on a residual mantle Bouguer anomaly map
 576 (Cannat et al., 2006). Panel c: seafloor is colored as in Figure 2 for ultramafic seafloor, and in brown
 577 for volcanic seafloor; magnetic anomalies 0 (open star), A1 and A2 (closed stars, grey when picking is
 578 ambiguous) as in (Cannat et al., 2006).

579

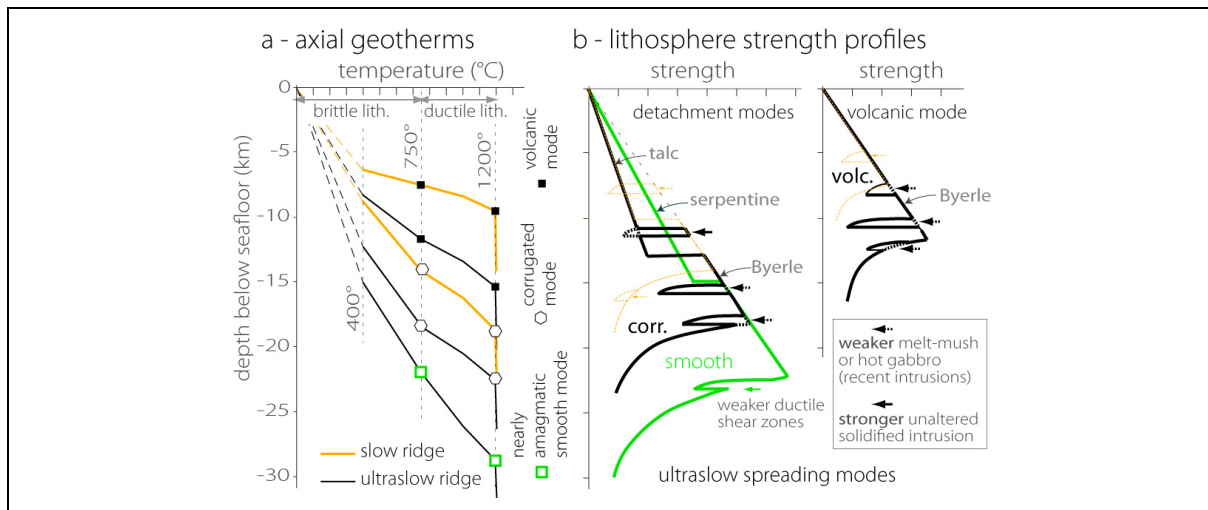


580 Figure 6. 3D perspective sketch of the axial region between cross-axis profiles 1 and 3 (in blue;
 581 location and tectonic interpretation of these profiles in Figure 5). The concept illustrated here is that

582 tectono-magmatic processes that accommodate plate divergence are tuned so that along-axis
 583 variations of melt supply are compensated by greater tectonic displacement on faults. In the nearly
 584 amagmatic configuration of profile 1, most plate divergence occurs at a single detachment fault, while
 585 in the more magmatically active configuration of profile 3, only 30 km away along-axis, the same total
 586 amount of divergence occurs through distributed faulting and magmatic injections. This sketch only
 587 goes down ~10 km into basement and therefore does not fully reach to the base of the lithosphere,
 588 particularly in the nearly amagmatic configuration, where it probably is >25km-deep (Schlindwein and
 589 Schmid, 2016). Full plate 2D sketches for the configurations of profiles 1 and 3 are shown in Figure 7.
 590



591 Figure 7. No vertical exaggeration, full plate 2D conceptual sketches of the ridge axis (a and b) and of
 592 axial geotherms (c) for across-axis profiles 1 and 3 (location in Figure 5). The base of the brittle
 593 lithosphere in a and b is drawn from constraints on the depth of seismicity (Schlindwein and Schmid,
 594 2016). The crust (grey) is a low density, low seismic velocity layer. It is sketched on the basis of gravity
 595 and seismic velocity constraints (Cannat et al., 2006; Momoh et al., 2017), and formed by the
 596 combination of magmatic flows, intrusions, fault damage, and serpentinization. For clarity, the axial
 597 sketches only show the most recent magmatic flows, intrusions, and infiltrations, and the most
 598 recently serpentinized domains. See text for explanations.



600 Figure 8. Conceptual sketches of axial geotherms (a) and lithosphere strength profiles (b) for the nearly
 601 amagmatic smooth seafloor detachment mode, the weakly magmatic corrugated detachment mode,
 602 and the magmatically more robust volcanic spreading mode, at slow and ultraslow ridges. Depth to
 603 the base of the brittle lithosphere is based on constraints on the depth of seismicity at the MAR and
 604 SWIR (Parnell-Turner et al., 2017; Schlindwein and Schmid, 2016; Wolfe et al., 1995; Yu et al., 2018).
 605 Thermal gradients in the lower lithosphere are inferred to be higher at higher melt supply (see Figure
 606 7c and text). Lithosphere strength (not scaled) is a function both of lithosphere thickness, and of two
 607 types of weakening mechanisms: hydrothermal alteration yielding weaker minerals (simplified here as
 608 a choice between serpentine or mechanically weaker talc; see text); and melt injection, which initially
 609 weakens the plate as the melt cools, then could make it locally stronger (if cutting through weak,
 610 hydrothermally altered exhumed mantle; see text). These weakening mechanisms differ between the
 611 3 spreading modes and are proposed to contribute to the transition from one mode to another at
 612 varying melt supply (see text).

613

614 REFERENCES

- 615 Andreani, M., Mével, C., Boullier, A.M., Escartín, J., 2007. Dynamic control on serpentine
 616 crystallization in veins: Constraints on hydration processes in oceanic peridotites.
 617 *Geochemistry, Geophysics, Geosystems* 8. <https://doi.org/10.1029/2006GC001373>
- 618 Boschi, C., Früh-Green, G.L., Escartín, J., 2006. Occurrence and significance of serpentinite-hosted,
 619 talc- and amphibole-rich fault rocks in modern oceanic settings and ophiolite complexes: An
 620 overview. *Ophioliti* 31, 129–140. <https://doi.org/10.4454/phioliti.v31i2.335>
- 621 Bronner, A., Sauter, D., Munsch, M., Carlut, J., Searle, R., Cannat, M., Manatschal, G., 2014.

622 Magnetic signature of large exhumed mantle domains of the Southwest Indian Ridge –
623 Results from a deep-tow geophysical survey over 0 to 11 Ma old seafloor. *Solid Earth* 5, 339–
624 354. <https://doi.org/10.5194/se-5-339-2014>

625 Buck, W.R., 1988. flexural rotation of normal faults. *Tectonics*.
626 <https://doi.org/10.1029/TC007i005p00959>

627 Buck, W.R., Lavier, L.L., Poliakov, A.N.B., 2005. Modes of faulting at mid-ocean ridges. *Nature* 434,
628 719–723. <https://doi.org/10.1038/nature03358>

629 Cann, J.R., Blackman, D.K., Smith, D.K., McAllister, E., Janssen, B., Mello, S., Avgerinos, E., Pascoe,
630 A.R., Escartin, J., 1997. Corrugated slip surfaces formed at ridge-transform intersections on the
631 Mid-Atlantic Ridge. *Nature* 385, 329–332. <https://doi.org/10.1038/385329a0>

632 Cannat, M., 1993. Emplacement of mantle rocks in the seafloor at mid-ocean ridges. *Journal of*
633 *Geophysical Research* 98, 4163–4172. <https://doi.org/10.1029/92JB02221>

634 Cannat, M., Céline, R.J., Fujimoto, H., 2003. Melt supply variations to a magma-poor ultra-slow
635 spreading ridge (Southwest Indian Ridge 61° to 69°E). *Geochemistry, Geophysics, Geosystems* 4,
636 1–21. <https://doi.org/10.1029/2002GC000480>

637 Cannat, M., Mangeney, A., Ondréas, H., Fouquet, Y., Normand, A., 2013. High-resolution bathymetry
638 reveals contrasting landslide activity shaping the walls of the Mid-Atlantic Ridge axial valley.
639 *Geochemistry, Geophysics, Geosystems* 14, 996–1011. <https://doi.org/10.1002/ggge.20056>

640 Cannat, M., Sauter, D., Bezos, A., Meyzen, C., Humler, E., Le Rigoleur, M., 2008. Spreading rate,
641 spreading obliquity, and melt supply at the ultraslow spreading Southwest Indian Ridge.
642 *Geochemistry, Geophysics, Geosystems*. <https://doi.org/10.1029/2007GC001676>

643 Cannat, M., Sauter, D., Escartín, J., Lavier, L., Picazo, S., 2009. Oceanic corrugated surfaces and the
644 strength of the axial lithosphere at slow spreading ridges. *Earth and Planetary Science Letters*
645 288, 174–183. <https://doi.org/10.1016/j.epsl.2009.09.020>

646 Cannat, M., Sauter, D., Mendel, V., Ruellan, E., Okino, K., Escartin, J., Combiér, V., Baala, M., 2006.
647 Modes of seafloor generation at a melt-poor ultraslow-spreading ridge. *Geology* 34, 605–608.
648 <https://doi.org/10.1130/G22486.1>

649 Chen, Y., Morgan, W.J., 1990. A Nonlinear Rheology Model for Mid-Ocean Ridge Axis Topography The
650 relative size of the decoupling chamber to the size lated to form the theory for the oceanic of
651 the plastic failure zone within the brittle plate determines the sphere and an iteration sch.
652 *Journal of Geophysical Research: Solid Earth* 95.

653 de Martin, B.J., Reves-Sohn, R.A., Canales, J.P., Humphris, S.E., 2007. Kinematics and geometry of
654 active detachment faulting beneath the Trans-Atlantic geotraverse (TAG) hydrothermal field on
655 the Mid-Atlantic Ridge. *Geology* 35, 711–714. <https://doi.org/10.1130/G23718A.1>

656 Detrick, R.S., Buhl, P., Vera, E., Mutter, J., Orcutt, J., Madsen, J., Brocher, T., 1987. Multi-channel
657 seismic imaging of a crustal magma chamber along the East Pacific Rise. *Nature*.
658 <https://doi.org/10.1038/326035a0>

659 Escartín, J., Mével, C., MacLeod, C.J., McCaig, A.M., 2003. Constraints on deformation conditions and
660 the origin of oceanic detachments: The Mid-Atlantic Ridge core complex at 15°45'N.
661 *Geochemistry, Geophysics, Geosystems*. <https://doi.org/10.1029/2002GC000472>

662 Escartín, J., Smith, D.K., Cann, J., Schouten, H., Langmuir, C.H., Escrig, S., 2008. Central role of
663 detachment faults in accretion of slow-spreading oceanic lithosphere. *Nature* 455, 790–794.
664 <https://doi.org/10.1038/nature07333>

665 Früh-Green, G.L., Connolly, J.A.D., Plas, A., Kelley, D.S., Grobéty, B., 2004. Serpentinization of oceanic
666 peridotites: Implications for geochemical cycles and biological activity. *Geophysical Monograph*
667 *Series* 144, 119–136. <https://doi.org/10.1029/144GM08>

668 Gillard, M., Autin, J., Manatschal, G., Sauter, D., Munschy, M., Schaming, M., 2015. Tectonomagmatic
669 evolution of the final stages of rifting along the deep conjugate Australian-Antarctic magma-
670 poor rifted margins: Constraints from seismic observations. *Tectonics*.
671 <https://doi.org/10.1002/2015TC003850>

672 Lavier, L.L., 2002. Half graben versus large-offset low-angle normal fault: Importance of keeping cool
673 during normal faulting. *Journal of Geophysical Research* 107, 2122.
674 <https://doi.org/10.1029/2001JB000513>

675 Lavier, L.L., Buck, W.R., Poliakov, A.N.B., 1999. Self-consistent rolling-hinge model for the evolution
676 of large-offset low-angle normal faults. *Geology* 27, 1127–1130. [https://doi.org/10.1130/0091-
677 7613\(1999\)027<1127:SCRHMF>2.3.CO;2](https://doi.org/10.1130/0091-7613(1999)027<1127:SCRHMF>2.3.CO;2)

678 Lin, J., Purdy, G.M., Schouten, H., Sempere, J.C., Zervas, C., 1990. Evidence from gravity data for
679 focused magmatic accretion along the Mid-Atlantic Ridge. *Nature*.
680 <https://doi.org/10.1038/344627a0>

681 Lowell, R.P., Farough, A., Hoover, J., Cummings, K., 2013. Characteristics of magma-driven
682 hydrothermal systems at oceanic spreading centers. *Geochemistry, Geophysics, Geosystems* 14,
683 1756–1770. <https://doi.org/10.1002/ggge.20109>

684 MacLeod, C.J., Searle, R.C., Murton, B.J., Casey, J.F., Mallows, C., Unsworth, S.C., Achenbach, K.L.,

685 Harris, M., 2009. Life cycle of oceanic core complexes. *Earth and Planetary Science Letters* 287,
686 333–344. <https://doi.org/10.1016/j.epsl.2009.08.016>

687 Minshull, T.A., Muller, M.R., White, R.S., 2006. Crustal structure of the Southwest Indian Ridge at
688 66°E: Seismic constraints. *Geophysical Journal International* 166, 135–147.
689 <https://doi.org/10.1111/j.1365-246X.2006.03001.x>

690 Momoh, E., Cannat, M., Watremez, L., Leroy, S., Singh, S.C., 2017. Quasi-3-D Seismic Reflection
691 Imaging and Wide-Angle Velocity Structure of Nearly Amagmatic Oceanic Lithosphere at the
692 Ultraslow-Spreading Southwest Indian Ridge. *Journal of Geophysical Research: Solid Earth* 122,
693 9511–9533. <https://doi.org/10.1002/2017JB014754>

694 Olive, J.A., Behn, M.D., Tucholke, B.E., 2010. The structure of oceanic core complexes controlled by
695 the depth distribution of magma emplacement. *Nature Geoscience* 3, 491–495.
696 <https://doi.org/10.1038/ngeo888>

697 Oufi, O., Cannat, M., Horen, H., 2002. Magnetic properties of variably serpentinized abyssal
698 peridotites. *Journal of Geophysical Research* 107, 2095. <https://doi.org/10.1029/2001JB000549>

699 Paquet, M., Cannat, M., Brunelli, D., Hamelin, C., Humler, E., 2016. Effect of melt/mantle interactions
700 on MORB chemistry at the easternmost Southwest Indian Ridge (61°–67°E). *Geochemistry,*
701 *Geophysics, Geosystems*. <https://doi.org/10.1002/2016GC006385>

702 Parnell-Turner, R., Sohn, R.A., Peirce, C., Reston, T.J., MacLeod, C.J., Searle, R.C., Simão, N.M., 2017.
703 Oceanic detachment faults generate compression in extension. *Geology* 45, 923–926.
704 <https://doi.org/10.1130/G39232.1>

705 Patriat, P., Segoufin, J., 1988. Reconstruction of the Central Indian Ocean. *Tectonophysics*.
706 [https://doi.org/10.1016/0040-1951\(88\)90267-3](https://doi.org/10.1016/0040-1951(88)90267-3)

707 Peron-Pinvidic, G., Manatschal, G., Osmundsen, P.T., 2013. Structural comparison of archetypal
708 Atlantic rifted margins: A review of observations and concepts. *Marine and Petroleum Geology*
709 43, 21–47. <https://doi.org/10.1016/j.marpetgeo.2013.02.002>

710 Picazo, S., Cannat, M., Delacour, A., Escartín, J., Rouméjon, S., Silantyev, S., 2012. Deformation
711 associated with the denudation of mantle-derived rocks at the Mid-Atlantic Ridge 13°–15°N: The
712 role of magmatic injections and hydrothermal alteration. *Geochemistry, Geophysics,*
713 *Geosystems*. <https://doi.org/10.1029/2012GC004121>

714 Püthe, C., Gerya, T., 2014. Dependence of mid-ocean ridge morphology on spreading rate in
715 numerical 3-D models. *Gondwana Research*. <https://doi.org/10.1016/j.gr.2013.04.005>

716 Reston, T., 2018. Flipping detachments: The kinematics of ultraslow spreading ridges. Earth and
717 Planetary Science Letters. <https://doi.org/10.1016/j.epsl.2018.09.032>

718 Reston, T.J., McDermott, K.G., 2011. Successive detachment faults and mantle unroofing at magma-
719 poor rifted margins. *Geology* 39, 1071–1074. <https://doi.org/10.1130/G32428.1>

720 Reston, T.J., Ranero, C.R., 2012. The 3-D geometry of detachment faulting at mid-ocean ridges.
721 *Geochemistry, Geophysics, Geosystems* 12, 1–19. <https://doi.org/10.1029/2011GC003666>

722 Rouméjon, S., Cannat, M., 2014. Serpentinization of mantle-derived peridotites at mid-ocean ridges:
723 Mesh texture development in the context of tectonic exhumation. *Geochemistry, Geophysics,*
724 *Geosystems*. <https://doi.org/10.1002/2013GC005148>

725 Rouméjon, S., Cannat, M., Agrinier, P., Godard, M., Andreani, M., 2014. Serpentinization and fluid
726 pathways in tectonically exhumed peridotites from the southwest Indian ridge (62–65°E).
727 *Journal of Petrology* 56, 703–734. <https://doi.org/10.1093/petrology/egv014>

728 Sauter, D., Cannat, M., Rouméjon, S., Andreani, M., Birot, D., Bronner, A., Brunelli, D., Carlut, J.,
729 Delacour, A., Guyader, V., MacLeod, C.J., Manatschal, G., Mendel, V., Ménez, B., Pasini, V.,
730 Ruellan, E., Searle, R., 2013. Continuous exhumation of mantle-derived rocks at the Southwest
731 Indian Ridge for 11 million years. *Nature Geoscience* 6, 314–320.
732 <https://doi.org/10.1038/ngeo1771>

733 Schindwein, V., Schmid, F., 2016. Mid-ocean-ridge seismicity reveals extreme types of ocean
734 lithosphere. *Nature* 535, 276–279. <https://doi.org/10.1038/nature18277>

735 Schroeder, T., John, B.E., 2004. Strain localization on an oceanic detachment fault system, Atlantis
736 Massif, 30°N, Mid-Atlantic Ridge. *Geochemistry, Geophysics, Geosystems* 5.
737 <https://doi.org/10.1029/2004GC000728>

738 Smith, D.K., Cann, J.R., 1999. Constructing the upper crust of the Mid-Atlantic Ridge: A
739 reinterpretation based on the Puna Ridge, Kilauea Volcano. *Journal of Geophysical Research:*
740 *Solid Earth* 104, 25379–25399. <https://doi.org/10.1029/1999JB900177>

741 Smith, D.K., Cann, J.R., Escartín, J., 2006. Widespread active detachment faulting and core complex
742 formation near 13°N on the Mid-Atlantic Ridge. *Nature* 442, 440–443.
743 <https://doi.org/10.1038/nature04950>

744 Standish, J.J., Dick, H.J.B., Michael, P.J., Melson, W.G., O’Hearn, T., 2008. MORB generation beneath
745 the ultraslow spreading Southwest Indian Ridge (9–25°E): Major element chemistry and the
746 importance of process versus source. *Geochemistry, Geophysics, Geosystems* 9.
747 <https://doi.org/10.1029/2008GC001959>

748 Tian, X., Choi, E., 2017. Effects of axially variable diking rates on faulting at slow spreading mid-ocean
749 ridges. *Earth and Planetary Science Letters* 458, 14–21.
750 <https://doi.org/10.1016/j.epsl.2016.10.033>

751 Tucholke, B.E., Behn, M.D., Buck, W.R., Lin, J., 2008. Role of melt supply in oceanic detachment
752 faulting and formation of megamullions. *Geology*. <https://doi.org/10.1130/G24639A.1>

753 Wolfe, C.J., Purdy, G.M., Toomey, D.R., Solomon, S.C., 1995. Microearthquake characteristics and
754 crustal velocity structure at 29°N on the Mid-Atlantic Ridge: The architecture of a slow
755 spreading segment. *Journal of Geophysical Research*. <https://doi.org/10.1029/95JB02399>

756 Yu, Z., Li, J., Niu, X., Rawlinson, N., Wang, W., Hu, H., Wei, X., Zhang, J., Lian, Y., 2018. Lithospheric
757 Structure and Tectonic Processes Constrained by Microearthquake Activity at the Central
758 Ultraslow-. *Journal of Geophysical Research : Solid Earth* 6247–6262.

759 Zhao, M., Qiu, X., Li, J., Sauter, D., Ruan, A., Chen, J., Cannat, M., Singh, S., Zhang, J., Wu, Z., Niu, X.,
760 2013. Three-dimensional seismic structure of the Dragon Flag oceanic core complex at the
761 ultraslow spreading Southwest Indian Ridge (49°39'E). *Geochemistry, Geophysics, Geosystems*
762 14, 4544–4563. <https://doi.org/10.1002/ggge.20264>

763

764